Chapter 23
Ni Addition Induced Changes in Structural, Magnetic, and Cationic Distribution of $Zn_{0.75-x}Ni_xMg_{0.15}Cu_{0.1}Fe_2O_4$ Nano-ferrite

Manvi Satalkar, Shashank Narayan Kane, Tetiana Tatarchuk, and João Pedro Araújo

23.1 Introduction

Nano-magnetic material with spinel structure containing two sub-lattices, tetrahedral A and octahedral B site, has become an important matter of study because of its variety of industrial and biomedical applications [1–8]. Spinel ferrites (SF) have turn into a prominent material of research mainly for addressing the basic correlation between the spinel crystal structure and magnetic properties. This basic relation between structural and magnetic properties can be studied via cationic distribution at A and B site [9, 10]. Distribution of cations on A and B site depends on the valency, ionic radii, presence of different cations (Zn^{2+}, Ni^{2+}, Mn^{2+}, Co^{2+}, Fe^{3+}), synthesis method, synthesis parameters [11], etc., which plays a decisive role in determining structural and magnetic properties [12] of SF.

Cationic distribution can be effectively used in tuning the magnetic properties of SF. The magnetization behavior of SF can be elucidated either by Néel's collinear two-sub-lattice model or by Yafet-Kittel three-sub-lattice model. According to Néel's model, the cationic magnetic moments on A and B sites are allied antiparallel

M. Satalkar · S. N. Kane (✉)
Magnetic Materials Laboratory, School of Physics, D. A. University, Indore, India

T. Tatarchuk
Department of Pure and Applied Chemistry, Vasyl Stefanyk Precarpathian National University, Ivano-Frankivsk, Ukraine

Educational and Scientific Center of Chemical Materials Science and Nanotechnology, Vasyl Stefanyk Precarpathian National University, Ivano-Frankivsk, Ukraine

J. P. Araújo
IFIMUP and IN-Institute of Nanoscience and Nanotechnology, Department of Physics and Astronomy, Faculty of Sciences, University of Porto, Porto, Portugal
e-mail: jearaujo@fc.up.pt

to each other forming a collinear structure [13, 14] with certain resultant magnetization $M = M_B − M_A$, where M_A and M_B are, respectively, magnetic moment of A and B site. But, according to Yafet-Kittel (Y-K) model, B sub-lattice can be divided into two sub-lattices, B_1 and B_2, having equal magnitude of magnetic moments, each canted oppositely at identical angle, α_{Y-K}. In this way, two sub-lattices B_1 and B_2 have triangular spin arrangement which becomes more significant with changing concentration and cationic redistribution.

Among other SF, most of the literature reports electromagnetic properties of Ni-Zn-Mg-Cu ferrite [15–19], but the magnetic properties of Zn-Ni-Mg-Cu spinel ferrite are less explored [16, 19–24]. Sujatha et al. [16] investigated Mg substituted ann. (powder, 500 °C/3 h.; pellets, 950 °C/1 h.) Ni-Cu-Zn ferrite. The results depict enhanced permeability, decrease in saturation magnetization (M_s), and dielectric losses at higher frequencies with Mg substitution in $Ni_{0.5−x}Mg_xCu_{0.05}Zn_{0.45}Fe_2O_4$ ($x = 0.1, 0.2, 0.3, 0.4$). Coercivity (H_c) and anisotropy constant (K_1) increase up to $x = 0.2$ and then reduce with increasing Mg content. Maximum initial permeability (μ_i) was obtained for $x = 0.1$. Abdullah Dar et al. [19] examined $Ni_{0.5−x}Cu_{0.2}Zn_{0.3}Mg_xFe_2O_4$ ($x = 0.0–0.4$) (900 °C/5 h) ferrite system, synthesized by sol-gel method. Results showed increased electrical resistivity, reduced H_c, and dielectric losses with Mg substitution. Mg doping leads to increase in M_s up to $x = 0.2$, and thereafter it starts to decrease with increase in Mg content. Sujatha et al. [20] explored Mg substituted ann. (powder, 500 °C/3 h.; pellets, 950 °C/1 h.) $Ni_{0.5}Cu_{0.05}Mg_xZn_{0.45−x}Fe_2O_4$ ($x = 0.09, 0.18, 0.27, 0.36, 0.45$). Results reveal decrease in M_s, μ_i and increase in H_c, K_1, Curie temperature (T_c) with increasing Mg content. Sujatha et al. [21] studied co-substitution effect of Mg, Zn of ann. (powder, 500 °C/3 h.; pellets, 950 °C/2 h.) $Ni_{0.5−2x}Mg_xCu_{0.05}Zn_{0.45+x}Fe_2O_4$ ($x = 0.0, 0.04, 0.08, 0.12, 0.16$) ferrite. Results demonstrate gradual decrease of M_s, H_c, K_1, dielectric constant, dielectric loss factor, improved permeability, and enhanced resistance of samples. Satalkar et al. [22] studied the synthesis, structural and soft magnetic properties, and cation distribution of asburnt $Zn_{0.8−x}Ni_xMg_{0.1}Cu_{0.1}Fe_2O_4$ ($x = 0.0–0.8$) ferrites prepared by sol-gel autocombustion method. The paper reports increase in 50 Hz and quasi-static coercivity and anisotropy constant values with nickel content. Best magnetization value of 25.04 emu/g was obtained for $x = 0.60$. Kane et al. [23] demonstrate the correlation between magnetic properties and cationic distribution of ann. (500 °C/3 h) $Zn_{0.85−x}Ni_xMg_{0.05}Cu_{0.1}Fe_2O_4$ ($x = 0.0–0.8$). The paper depicts decrease in experimental, theoretical lattice constant ($a_{exp.}$, $a_{th.}$), specific surface area (S), and the distances between cations (Me-Me) (b, c, d, e, f) with increase in Ni doping. H_c and M_s of Zn-Ni-Mg-Cu ferrite ranges between 0.97–167.5 Oe and 47.63–136.93 $Am^2kg^{−1}$, respectively, signifying the soft character of annealed samples. The paper shows similar trend of M_s, Néel/experimental magnetic moment ($n_B{}^N$, $n_B{}^e$) with Ni content (x) which establishes the Néel's two-sub-lattice model of ferrimagnetism in ann. (500 °C/3 h) $Zn_{0.7−x}Ni_xMg_{0.2}Cu_{0.1}Fe_2O_4$ nano-ferrite. Furthermore the role of cationic distribution in determining magnetic properties

of $Zn_{0.7-x}Ni_xMg_{0.2}Cu_{0.1}Fe_2O_4$ ($x = 0.0$–0.7) nano-ferrite is presented in [24]. The magnetic properties M_s (43.2–69.9 Am^2/kg) and $n_B{}^N$ (1.74–2.86 μ_B) increase up to $x = 0.42$, but at higher values of Ni content ($0.42 < x \leq 0.70$) M_s and $n_B{}^N$ decrease, but coercivity (16.3–131.1 Oe) increases constantly with increasing Ni content. Zero values of Yafet-Kittel angle ($\alpha_{Y\text{-}K}$) suggest the presence of Néel-type magnetic ordering in $Zn_{0.7-x}Ni_xMg_{0.2}Cu_{0.1}Fe_2O_4$.

The above available literature [16, 19–24] on Zn-/Mg-doped mixed Zn-Ni-Mg-Cu SF explains the variation of magnetization with the doping content on the basis of Néel's two-sub-lattice model of ferrimagnetism, but up till now no literature on Ni-doped Zn-Mg-Cu SF is available which shows the presence of Yafet-Kittel three-sub-lattice model. Some reports are available [25–30] which shows the presence of Y-K type of magnetic ordering for high doping content. Thus, magnetic ordering also depends on the effect of doping concentration of the cation as also observed in [25–30]. Hence, it becomes important to study the effect of dopant on the structural, magnetic properties of SF.

Therefore, the aim of the present work is to look into the effect of Ni content on structural, magnetic properties of $Zn_{0.75-x}Ni_xMg_{0.15}Cu_{0.1}Fe_2O_4$ ferrite, synthesized by sol-gel auto-combustion.

23.2   Materials and Methods

23.2.1   Materials

AR-grade zinc nitrate, $Zn(NO_3)_2.6H_2O$; nickel acetate, $Ni(CH_3COO)_2.4H_2O$; magnesium acetate, $Mg(CH_3COO)_2 \cdot 4H_2O$; copper nitrate, $Cu(NO_3)_2.3H_2O$; and ferric nitrate, $Fe(NO_3)_3.9H_2O$, were used for the synthesis of $Zn_{0.75-x}Ni_xMg_{0.15}Cu_{0.1}Fe_2O_4$ ($x = 0.00, 0.15, 0.30, 0.45, 0.60,$ and 0.75) spinel ferrite.

23.2.2   Material Synthesis

$Zn_{0.75-x}Ni_xMg_{0.15}Cu_{0.1}Fe_2O_4$ ferrites were synthesized by sol-gel auto-combustion method. Stoichiometric amounts of citrate-nitrate/acetate precursors were mixed with citric acid (in the molar ratio 1:1). Citric acid has a dual function: *initially it acts as a chelator and then as a fuel* [31]. Synthesis was done by dissolving all the precursors in stoichiometric ratio in deionized water, and then ammonia solution (NH_4OH) was added to maintain the pH at 7 by continuous stirring. Now the solution was heated at 120 °C in air till the loose powder (fluffy) was formed called as "dry gel or as-burnt powder" which was then annealed at 500 °C for 3 h in air.

23.2.3   Characterizations

Room temperature structural properties of annealed powders were examined by X-ray diffraction (XRD) using Cu-K$_\alpha$ radiation (wavelength 'λ' =0.1540562 nm) in θ–2θ configuration (step size of 0.019° and a scanning rate of 1.14 degree/minute), equipped by a fast counting Bruker LynxEye detector, with silicon strip technology. Elemental, quantitative analysis of surface morphology of Zn-Ni-Mg-Cu ferrite samples was performed by energy-dispersive X-ray analysis (EDAX, INCA-OXFORD) and scanning electron microscope (SEM, JEOL JSM-6390LV). Room temperature magnetization studies were done via SQUID magnetometer (Quantum Design MPMS-5S) with a maximum applied field ($H_{\mathrm{max.}}$) of $\pm$ 5 tesla. The magnetic properties, saturation magnetization (M_s), squareness ratio/reduced magnetization ($M_\mathrm{r}/M_\mathrm{s}$), and coercivity ($H_\mathrm{c}$), have been elucidated from hysteresis loops.

23.3   Results and Discussions

23.3.1   Structural Properties

X-ray diffraction (XRD) patterns of Ni^{2+}-doped annealed 500 °C/3 h Zn$_{0.75-x}$Ni$_x$ Mg$_{0.15}$Cu$_{0.1}$Fe$_2$O$_4$ (x = 0.00–0.75) ferrite system is depicted in Fig. 23.1a. Figure 23.1b, c, respectively, illustrates the Rietveld refinement for the composition x = 0.00 and x = 0.75, done via MAUD (Material Analysis Using Diffraction) software [32]. XRD confirms the single-phase spinel structure (JCPDS card No. 08-0234), signifying the cations solubility within their individual lattice sites. Structural parameters, experimental lattice parameter ($a_{\mathrm{exp.}}$), Scherrer's grain diameter (D), hopping length at A (L_A) and B (L_B) site, and specific surface area (S) of the studied samples, were calculated as described in [22, 33] and are specified in Table 23.1. Observed changes in $a_{\mathrm{exp.}}$ L_A and L_B can be accredited to difference in ionic radii of Zn^{2+} (0.060 nm) and Ni^{2+} (0.055 nm) ion. Lattice parameter of Zn$_{0.75-x}$Ni$_x$Mg$_{0.15}$Cu$_{0.1}$Fe$_2$O$_4$ ferrite system initially increases for x = 0.15 and decreases up to x = 0.60 and again increases for x = 0.75. The value should decrease with the substitution of larger Zn^{2+} (0.060 nm) ion by smaller Ni^{2+} (0.055 nm) ion. But in present system, $a_{\mathrm{exp.}}$ of Ni^{2+} substituted Zn-Mg-Cu ferrite shows a non-monotonic behavior (common in systems which are not entirely normal or inverse [34, 35]) with increasing Ni^{2+} content, violating Vegard's law [36]. Scherrer's grain diameter (D) of the nano-phase synthesized particles initially increases for x = 0.15, decreases up to x = 0.45, and thereafter again increases up to x = 0.75. Though the synthesis was done under same conditions, the observed grain size is not same for all Ni^{2+}-doped samples. Such non-monotonic behavior of D with increasing Ni concentration may be due to reaction condition, which initially favored the particle growth, and when Ni content is increased further, the creation of new nuclei occurs without any increase in particle size. At higher Ni content (0.45 < x $\leq$ 0.75),

Fig. 23.1 (**a**) XRD pattern of annealed $Zn_{0.75-x}Ni_xMg_{0.15}Cu_{0.1}Fe_2O_4$ system. Representative Rietveld refinement for (**b**) $x = 0.00$ and (**c**) $x = 0.75$
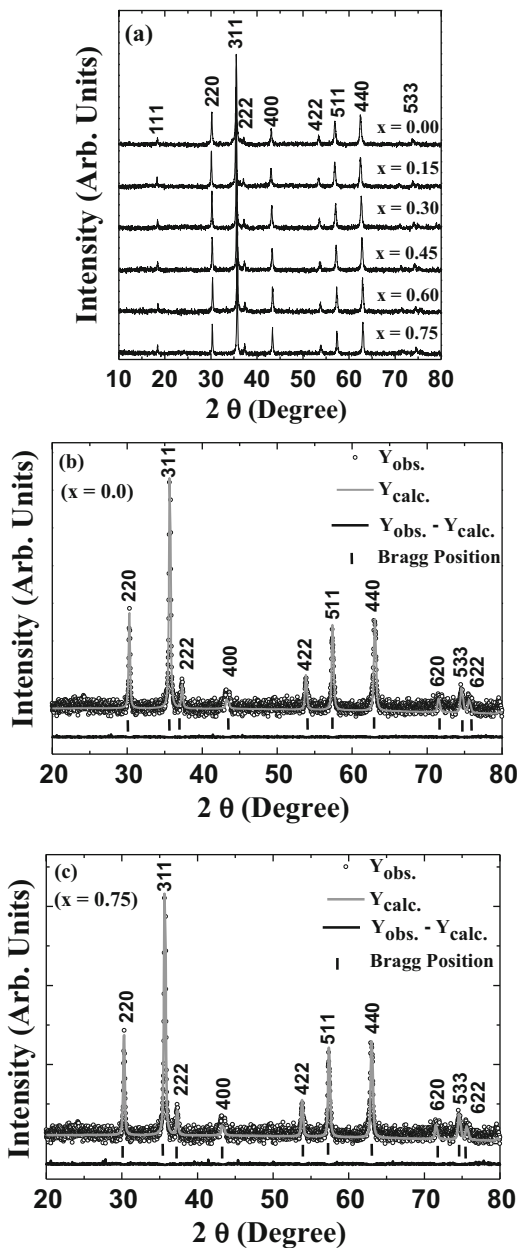
again the reaction condition favors the particle growth, attributed to different dry gel formation time. High specific surface areas (*S*) of particles are tremendously important for assorted catalytic processes. In general, high surface areas suggest small particle sizes. The smaller the particle size, the larger the surface area. *S*

Table 23.1 Lattice parameter ($a_{exp.}$), hopping length for A site (L_A) and B site (L_B), Scherrer's grain diameter (D), specific surface area (S), and uniform strain (ε_u) with Ni content (x) of ann. 500 °C/3 h $Zn_{0.75-x}Ni_xMg_{0.15}Cu_{0.1}Fe_2O_4$ spinel ferrite

x	a (nm)	L_A (nm)	L_B (nm)	D (nm)	S (m^2/g)	$\varepsilon_u \times 10^{-3}$
0.00	0.8380	0.3629	0.2963	41.40	27.35	–
0.15	0.8397	0.3636	0.2969	50.89	22.48	1.9786
0.30	0.8385	0.3631	0.2965	49.67	23.04	3.9573
0.45	0.8349	0.3615	0.2952	47.09	24.09	−3.9573
0.60	0.8328	0.3606	0.2944	54.99	20.56	−6.3316
0.75	0.8336	0.3610	0.2947	56.73	20.08	−5.5402

of Zn-Ni-Mg-Cu ferrite system initially decreases for $x = 0.15$, increases up to $x = 0.45$, and again decreases thereafter. Increase and decrease in S can be ascribed to decrease and increase of D, respectively. Annealed particles are less suitable for catalytic application than the as-burnt particles (without any thermal/sintering treatment) because of their larger grain size. The uniform strain (ε_u) for the studied samples was calculated using the expression [37]. Table 23.1 depicts the presence of compressive and tensile strain in the annealed Zn-Ni-Mg-Cu ferrite. The variation in the strain value can be attributed to the crystallinity of the synthesized samples.

23.3.2 Cationic Distribution

Cationic distribution of all the studied samples was determined by analyzing the XRD pattern, employing Bertaut method [38–41]. Cationic distribution of such mixed ferrite determined from the XRD intensities is also reported earlier in many reports [22–24, 42–46]. XRD intensity depends on the atomic position in spinel unit cell, whereas XRD peak position relies on size and shape of unit cell. This method uses a pair of reflections, 400/422 and 220/400, according to expression: $\frac{I_{hkl}^{obs}}{I_{h'k'l'}^{obs}} = \frac{I_{hkl}^{cal}}{I_{h'k'l'}^{cal}}$ where $I_{hkl}{}^{obs}$ and $I_{hkl}{}^{cal}$ are, respectively, the observed and calculated intensities for the reflection (hkl). These ratios were evaluated for several combinations of cationic distribution at A and B sites as described in [41]. The finest cationic distribution among A and B sites for which theoretical and experimental ratios agree clearly was taken. Cationic distribution of $Zn_{0.75-x}Ni_xMg_{0.15}Cu_{0.1}Fe_2O_4$ spinel ferrite and calculated, observed intensity ratio for the planes, 400/422 and 220/400, are given in Table 23.2. Close matching of observed and calculated intensity ratio of 400/422 and 220/400 suggests an appropriate distribution of cations among A and B site. Table 23.2 also summarizes the occupation of Zn^{2+}, Ni^{2+}, Mg^{2+}, Cu^{2+}, and Fe^{3+} ions on A and B site. Cationic distribution of Mg^{2+} ions on A and B site is independent of Ni doping. Cu^{2+} ions are present only at B site for all values of x, but, for $x = 0.00$, Cu^{2+} ions are equally distributed at A and B site. Ni^{2+} ions

Table 23.2 Cation distribution (for A and B site) and observed, calculated intensity ratios for $I_{400/422}$, $I_{220/400}$ of $Zn_{0.75-x}Ni_xMg_{0.15}Cu_{0.1}Fe_2O_4$ as a function of Ni content (x)

		$I_{400/422}$		$I_{220/400}$			
x	Cation distribution	Cal.	Obs.	Cal.	Obs.	r_A (nm)	r_B (nm)
0.00	$(Zn^{2+}_{0.07}Cu^{2+}_{0.05}Fe^{3+}_{0.88})_A$ $[Zn^{2+}_{0.68}Mg^{2+}_{0.15}Cu_{0.05}Fe^{3+}_{1.12}]_B$	1.70	1.72	1.61	1.60	0.0502	0.0685
0.15	$(Zn^{2+}_{0.1}Ni^{2+}_{0.15}Fe^{3+}_{0.75})_A$ $[Zn^{2+}_{0.5}Mg^{2+}_{0.15}Cu_{0.1}Fe^{3+}_{1.25}]_B$	1.44	1.41	1.67	1.65	0.0510	0.0679
0.30	$(Zn^{2+}_{0.06}Ni^{2+}_{0.2}Fe^{3+}_{0.74})_A$ $[Zn^{2+}_{0.39}Ni^{2+}_{0.1}Mg^{2+}_{0.15}Cu^{2+}_{0.1}Fe^{3+}_{1.26}]_B$	1.59	1.59	1.78	1.73	0.0509	0.0676
0.45	$(Ni^{2+}_{0.33}Fe^{3+}_{0.67})_A$ $[Zn^{2+}_{0.3}Ni^{2+}_{0.12}Mg^{2+}_{0.15}Cu_{0.1}Fe^{3+}_{1.33}]_B$	1.65	1.63	1.79	1.76	0.0510	0.0672
0.60	$(Ni^{2+}_{0.25}Fe^{3+}_{0.75})_A$ $[Zn^{2+}_{0.15}Ni^{2+}_{0.35}Mg^{2+}_{0.15}Cu_{0.1}Fe^{3+}_{1.25}]_B$	1.69	1.68	1.65	1.63	0.0505	0.0669
0.75	$(Ni^{2+}_{0.05}Fe^{3+}_{0.95})_A$ $[Ni^{2+}_{0.7}Mg^{2+}_{0.15}Cu^{2+}_{0.1}Fe^{3+}_{1.05}]_B$	1.74	1.75	1.71	1.71	0.0493	0.0671

occupy only A site for $x = 0.15$, but, with further increase in doping content (x), Ni^{2+} ions occupy both A and B site. Also the concentration of Ni^{2+} ions increases on A site with x; however, for $x = 0.60$–0.75, Ni^{2+} ions decrease. Ni doping also decreases Zn^{2+} ions on B site. Zn^{2+} ions are present both at A and B site, except for higher values of Ni content ($0.45 \leq x \leq 0.75$) where Zn^{2+} ions are completely migrated to B site. Ni doping also decreases Fe^{3+} ions on A and increases on B site up to $x = 0.45$ and then increases for A and decreases for B site thereafter. The cationic distribution in the present system shows the same trend as observed earlier [22–24, 47–50]. Using the obtained cation distribution, A and B site ionic radii (r_A, r_B) were calculated using the relation given in [41]. Ni content dependence of A (r_A) and B (r_B) site ionic radii is depicted in Table 23.2. Not much change is observed in the values of r_A except for $x = 0.15$ which can be accredited to the sudden increase in larger Zn^{2+} ion (0.06 nm) by a large amount and decrease of smaller Fe^{3+} (0.049 nm) ions on A site. But the values of r_B show considerable changes with Ni content (x). Observed decreases in r_B with x are due to continuous decrease in larger Zn^{2+} ion (0.074 nm) and increase of smaller Ni^{2+} ion (0.069 nm) on B site.

For a better understanding of Zn-Ni-Mg-Cu ferrite, spinel structure tetrahedral and octahedral bond length (R_A, R_B), oxygen parameter ($u^{\overline{4}3m}$), shared tetrahedral edge length (d_{AE}), and shared and unshared octahedral edge length (d_{BE}, d_{BEu}) were also calculated and are given in Table 23.3. Oxygen positional parameter or anion parameter ($u^{\overline{4}3m}$) is calculated using r_A and $a_{exp.}$ values via the expression [43]. Oxygen parameter represents the movement of O^{2-} ion due to substitution of Ni^{2+} cation at A site. u parameter reflects modification of the spinel structure to adjust differences in the radius ratio of the cation in A and B sites. Values of $u^{\overline{4}3m}$ parameter calculated for different compositions specified in Table 23.3 show an increase with x

Table 23.3 Ni content dependence of oxygen positional parameter ($u^{\overline{4}3m}$), shared tetrahedral edge length (d_{AE}), shared (d_{BE}) and unshared octahedral edge length (d_{BEu}), and tetrahedral (R_A) and octahedral bond length (R_B) for ann. (500 °C/3 h) $Zn_{0.75-x}Ni_xMg_{0.15}Cu_{0.1}Fe_2O_4$ system

x	$u^{\overline{4}3m}$	d_{AE} (nm)	d_{BE} (nm)	d_{BEu} (nm)	R_A (nm)	R_B (nm)
0.00	0.3796	0.3073	0.2853	0.2964	0.1882	0.2056
0.15	0.3799	0.3086	0.2851	0.2970	0.1890	0.2058
0.30	0.3800	0.3084	0.2845	0.2966	0.1889	0.2054
0.45	0.3807	0.3086	0.2818	0.2953	0.1890	0.2040
0.60	0.3806	0.3078	0.2811	0.2946	0.1885	0.2035
0.75	0.3797	0.3058	0.2835	0.2949	0.1873	0.2045

up to $x = 0.45$ and reduces for $0.45 < x \leq 0.75$. For ideal cubic closed packed spinel structure, $u_{ideal}^{\overline{4}3m} = 0.375$ [43]. The calculated u parameter values are greater than the ideal value ($u_{ideal}^{\overline{4}3m} = 0.375$) for entire $Zn_{0.75-x}Ni_xMg_{0.15}Cu_{0.1}Fe_2O_4$ nano-ferrite revealing distortion in the spinel structure. $u^{\overline{4}3m}$ and $a_{exp.}$ values were also utilized in the calculation of other cation distribution parameters, demonstrated in Table 23.3: d_{AE}, d_{BE}, d_{BEu}, R_A, and R_B using the relations [51]. The observed variation in tetrahedral bond length (R_A) and shared tetrahedral edge (d_{AE}) is in accordance with the changes in the ionic radii of A site (r_A) with Ni content (x). Decrease in octahedral bond length (R_B) and shared and unshared octahedral edge (d_{BE}, d_{BEu}) with Ni doping is accredited to the replacement of larger ion (Zn^{2+}) by smaller ion (Ni^{2+}).

23.3.3 SEM, EDAX

Representative low-magnification (LM) and high-magnification (HM) SEM images for the composition $x = 0.00$ and $x = 0.45$ shown in Fig. 23.2 depict difference in surface morphology, porosity, and particle agglomeration with diverse shapes and sizes. This difference signifies that presence or absence of Ni ion in Zn-Mg-Cu ferrite plays an imperative role in microstructure of prepared spinel ferrite. The encircled area of SEM images represents the magnified region of the image. The non-connected spherical pores are noticeably visible in the LM and HM SEM images of $x = 0.00$ with dissimilar pore sizes (555.70, 768.37, and 1.30 µm), which are missing for $x = 0.45$. The HM SEM image of the sample with $x = 0.45$ shows large particle clusters with a planar and homogeneous surface. Pores present in sample, $x = 0.00$, are accredited to the liberation of large quantity of gases during combustion process [52], which would also get influenced by different amounts of nitrate/acetate salts of Zn, Ni, Mg, Cu, and Fe ions and citric acid used for synthesizing the studied samples [53], leading to changes in the pore sizes. Pores affect saturation magnetization (M_s), grain size (D), and surface area (S) of the
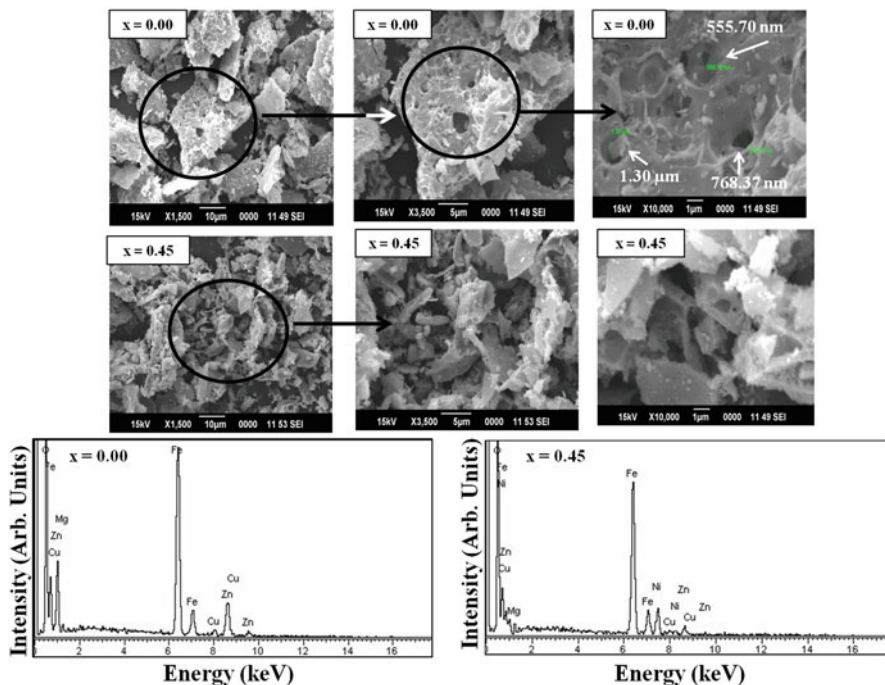
Fig. 23.2 SEM microstructures and EDAX of $Zn_{0.75-x}Ni_xMg_{0.15}Cu_{0.1}Fe_2O_4$ system for $x = 0.00$ and 0.45

sample [54, 55]. The sample with $x = 0.00$ shows the lowest value of M_s (27.22 Am^2/kg), and the sample with $x = 0.45$ exhibits the highest M_s (69.78 Am^2/kg). Pores operate as pinning core for electron spins and work as a demagnetizing field generator and, hence, reduce M_s as reported in earlier studies [54]. Occurrence of pores in the sample: $x = 0.00$ decreases D and increases S of the particles as compared with that of the sample: $x = 0.45$ (which is clearly seen in Table 23.1). Low value of D (for $x = 0.00$ than for $x = 0.45$) is due to the presence of pores which neutralizes the driving force for grain boundary movement and increases thickness of the grain boundary, and, hence, D decreases and S increases. Such porous structure with large surface area can be used in catalytic applications and as adsorbents [54, 56].

Elemental and quantitative analysis of the composition with $x = 0.00$ and $x = 0.45$ has been done using EDAX technique. EDAX spectra represented in Fig. 23.2 confirm the existence of all elements (Zn, Ni, Mg, Cu, Fe, O) in samples. The EDAX results distinctly indicate that all the precursors are very well reacted with each other to finally form the desired ferrite composition. The quantitative analysis of elements obtained from EDAX spectrum shows atomic and weight percentages of Zn, Ni, Mg, Cu, Fe, and O in Table 23.4. The close values of

Table 23.4 Weight %, atomic %, experimental Me/Fe molar ratio (Me/Fe)^{exp}, and theoretical Me/Fe molar ratio (Me/Fe)$^{th.}$ of the elements Zn, Ni, Mg, Cu, Fe, and O present in $Zn_{0.75-x}Ni_xMg_{0.15}Cu_{0.1}Fe_2O_4$ ($x = 0.00, 0.45$) system obtained from EDS analysis

Element	Weight %	Atomic %	(Me/Fe)$^{exp.}$	(Me/Fe)$^{th.}$
$x = 0.0$				
O	27.90	56.64	–	–
Mg	1.54	2.43	0.08	0.08
Fe	47.52	28.94	1	1
Zn	20.28	10.60	0.37	0.38
Cu	2.76	1.39	0.05	0.05
Total	**100.00**	**100.00**		
$x = 0.45$				
O	28.61	57.13	–	–
Mg	1.56	2.03	0.07	0.08
Fe	48.12	28.70	1	1
Ni	11.18	6.25	0.22	0.23
Cu	2.26	1.54	0.05	0.05
Zn	8.27	4.35	0.15	0.15
Total	**100.00**	**100.00**		

experimental and theoretical Me/Fe molar ratio (shown in Table 23.4) further confirm the homogeneous distribution of all the elements in the sample.

23.3.4 Magnetic Properties

Figure 23.3 shows room temperature hysteresis loops of the studied samples. Saturation magnetization (M_s) of Zn-Ni-Mg-Cu spinel ferrite is determined from M-H curve. But M_s for $x = 0.00$ and 0.15 is obtained by plotting M versus 1/H curve and extrapolating the data to 1/H = 0 [11] as samples are not saturated even at $H_{max.}$ of 5 tesla. The superparamagnetic behavior observed for $x = 0.00$ and 0.15 samples signifies that the magneto-crystalline anisotropy energy has been overcome by thermal energy. The samples are able to sustain magnetic ordering and show soft ferrimagnetic behavior due to enhancement of the magneto-crystalline anisotropy by the substitution of soft magnetic Ni^{2+} ions. Similar soft magnetic behavior in Zn-Ni-Mg-Cu ferrites has also been reported in literature [23, 24].

The magnetic parameters, Néel and experimental magnetic moment (n^e_N, n^e_B) μ_B, saturation magnetization (M_s), and Yafet-Kittle angle (α_{Y-K}), are illustrated in Table 23.5. Magnetization is influenced by both extrinsic and inherent parameters such as magneto-crystalline anisotropy constant, grain size, A-B exchange interactions, and site occupancy of cations [57]. Fluctuation in grain size also influences the magnetization due to domain wall movement under the action of magnetic field. The overall value of magnetization obtained is a result of the contribution of all the factors depending upon ferrite composition.

Fig. 23.3 Variation of room temperature magnetization with applied magnetic field
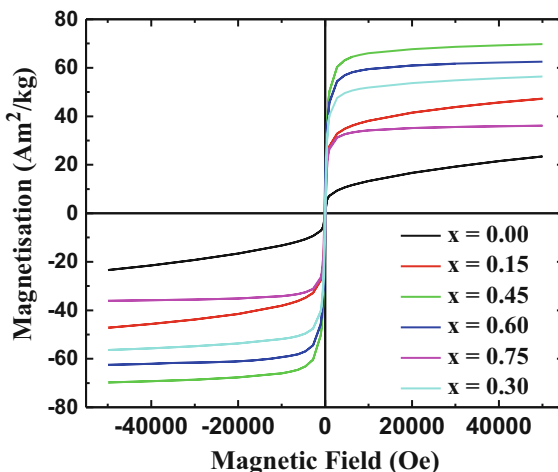

Table 23.5 Variation of magnetic parameters: Néel and experimental magnetic moment (n^e_N, n^e_B) μ_B, saturation magnetization (M_s), and Yafet-Kittel angle (α_{Y-K}) with Ni content (x) for $Zn_{0.75-x}Ni_xMg_{0.15}Cu_{0.1}Fe_2O_4$ (ann. 500 °C/3 h) system

x	n^e_N (μ_B)	n^e_B (μ_B)	M_s (Am^2/Kg)	α_{Y-K} (degree)
0.00	1.20	1.14	27.22	7.48
0.15	2.30	2.11	50.49	13.38
0.30	2.50	2.35	56.41	11.52
0.45	2.98	2.90	69.78	7.78
0.60	2.80	2.58	62.55	13.60
0.75	1.90	1.49	36.11	19.93

Perusal of Table 23.5 shows that Néel and experimental magnetic moment (calculated by using the expression [13]) and saturation magnetization initially enhance with Ni content up to $x = 0.45$ and then decrease for $0.45 < x \leq 0.75$, accredited to the occupation of cations as also explained earlier in [22–24, 51]. Magnetization of Zn-Ni-Mg-Cu ferrite mainly resides on the Ni^{2+} ($2\mu_B$) and Fe^{3+} ($5\mu_B$) ions because Zn^{2+} and Mg^{2+} ions are diamagnetic with 0 magnetic moment, and the percentage of occupied Cu^{2+} ($1\mu_B$) ions is constant at B site as the dopant ($Ni(x)$) is introduced in the spinel structure. With increasing Ni, up to $= 0.45$, Ni^{2+} ions force Fe^{3+} ions to migrate from A to B site; thus, Fe^{3+} ions on B site increase which in turn increase B site magnetic moment (M_B) and decrease A site magnetic moment (M_A), and therefore, the magnetization increases. Thus the saturation magnetization of Zn-Ni-Mg-Cu ferrite linearly depends on the content of Fe^{3+} ions on B site (shown in Fig. 23.4). Highest value of magnetization (69.78 Am^2/kg) is obtained for $x = 0.45$. When Zn^{2+} are completely substituted by Ni^{2+} ions (for $x = 0.75$), Ni^{2+} ions push Fe^{3+} ions from B to A site, resulting in decrease of M_s of the system.

Fig. 23.4 Variation of saturation magnetization (M_s) with Fe^{3+} ions on B site (Fe^{3+}(B)). Inset: variation of M_s with oxygen parameter ($u^{\overline{4}3m}$)
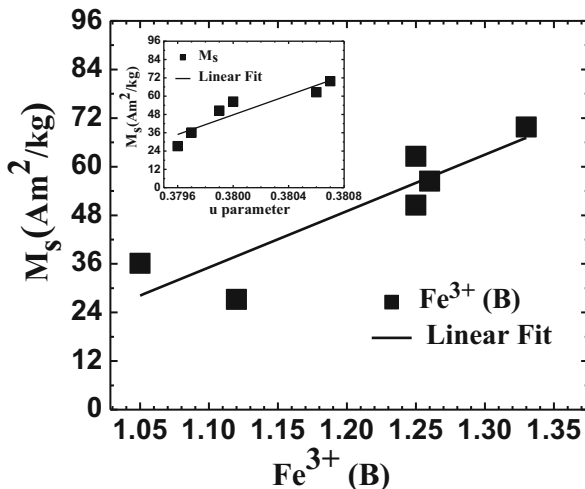
The magnetization behavior with different Ni concentration can also be explained by Yafet-Kittel three-sub-lattice model. The non-zero Y-K angles for $Zn_{0.75-x}Ni_xMg_{0.15}Cu_{0.1}Fe_2O_4$ ferrite given in Table 23.5 suggest the presence of non-collinear spin structure on B site, i.e., existence of Yafet-Kittel model [58]. According to Yafet-Kittel model, the octahedral lattice (B) of spinel can be separated into two sub-lattices, B_1 and B_2, with equal magnitude of magnetic moments, canted oppositely at the identical angle α_{Y-K}, known as Y-K angle and calculated as given in [26]. In this way, two sub-lattices, B_1 and B_2, have the triangular spin arrangement. Non-collinear magnetic ordering is also reported earlier for different systems [25–30]. α_{Y-K} initially increases for $x = 0.15$, decreases up to $x = 0.45$, and then finally increases for $0.45 < x \leq 0.75$ with increase in Ni content (x). Decrease in Y-K angle signifies decrease in spin canting at B site because of increase in A-B super exchange interaction, and increase of Y-K angle suggests increases of B-B interaction due to increase in spin canting at B site.

Observed linear variation (represented in Fig. 23.4 inset) of M_s with $u^{\overline{4}3m}$ can also be attributed due to changes in $u43m$ values. Based on the linear variation between M_s and $u^{\overline{4}3m}$, one can propose the following empirical relations: $M_s = Au^{\overline{4}3m} + B$ [59], where A and B are fitting constants with values, respectively, 12,186 and −32,193. This variation noticeably illustrates that $u^{\overline{4}3m}$ also contributes resolutely in determining M_s of the studied Zn-Ni-Mg-Cu ferrite. It is worth noting that increase of M_s with $u^{\overline{4}3m}$ is ascribed to higher distortion in the spinel structure, expected to affect the magnetization.
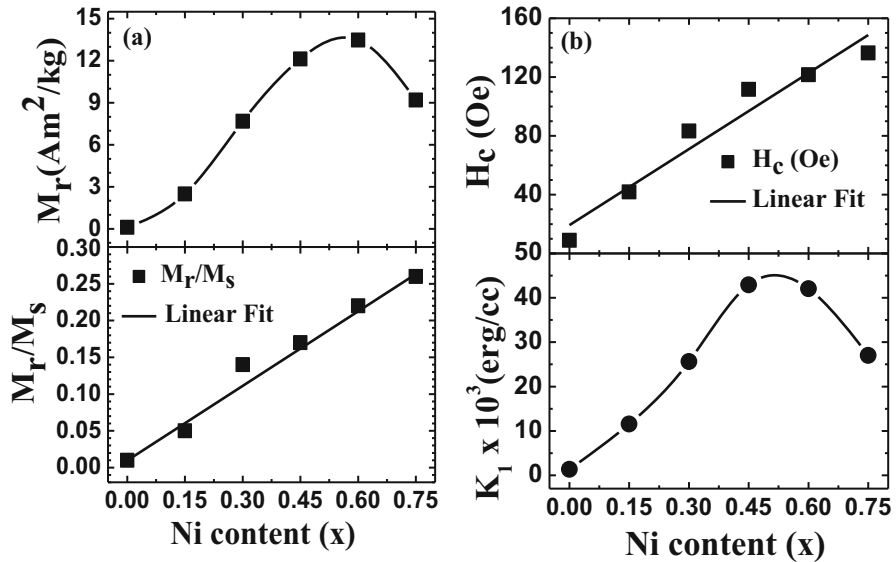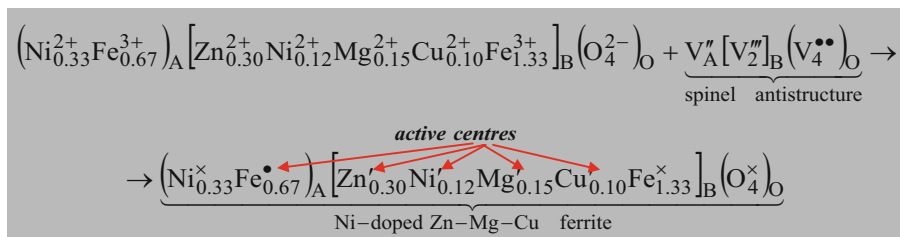
Fig. 23.5 (**a**) Ni content dependence of remanent magnetization (M_r) and squareness ratio (M_r/M_s). (**b**) Ni content dependence of coercivity (H_c) and magneto-crystalline anisotropy constant (K_1) for $Zn_{0.75-x}Ni_xMg_{0.15}Cu_{0.1}Fe_2O_4$

Variation of squareness ratio or reduced remanent magnetization (M_r/M_s) and remanent magnetization (M_R) with Ni content is specified in Fig. 23.5a. M_r/M_s and M_R values, respectively, range between 0.01–0.26 and 0.11–13.47 Am^2/kg. M_r/M_s values increase continuously with Ni content. M_R increases up to $x = 0.45$ and decreases thereafter. The variation in M_R is attributed to the changes in magnetization of the system [52], and it can be explained on the basis of cationic redistribution among A and B site [60] (as described for M_s). Variation of magnetic parameters, magneto-crystalline anisotropy constant (K_1) and coercivity (H_c), is given in Fig. 23.5b. The coercivity of polycrystalline ferrite depends on K_1. When Zn^{2+} ions are replaced by Ni^{2+} ions, magneto-crystalline anisotropy increases because the anisotropy constant value of Ni-ferrite is greater than Zn ferrite [13], and hence, H_c increases. Since K_1 of $NiFe_2O_4$ is greater than $ZnFe_2O_4$ [13] and when Zn^{2+} ions are replaced by Ni^{2+} ions, increase in K_1 is observed (clearly seen in Fig. 23.5b). But for $0.45 < x \leq 0.75$, K_1 decreases, which can be elucidated by single-ion anisotropy model [52]. According to this model, Fe^{3+} ions on A and B site contribute to anisotropy energy. K_1 value is then given by comparative combination A site Fe^{3+} ions with positive anisotropy which is compensated by B site Fe^{3+} ions with negative anisotropy. For $0.45 < x \leq 0.75$, negative contribution of B site Fe^{3+} ions increases, and positive contribution of A site Fe^{3+} ions decreases, which in turn decreases K_1.

23.3.5 Antistructural Modeling

Antistructural modeling is a new approach, which lets us predict the nature of the active surface centers. It is based on the superposition of the crystal structure with spinel antistructure $V''_A[V'''_2]_B(V_4^{\bullet\bullet})_O$, where V''_A is negatively charged tetrahedral cationic vacancy, V'''_B is negatively charged octahedral cationic vacancy, and $V_O^{\bullet\bullet}$ is positively charged oxygen vacancy. The markings '', ''' (negative charge) and •• (positive charge) correspond to the electronic charge of the species as regards the sites in the spinel lattice. So each cation from A site interacts with tetrahedral cationic vacancy V''_A, each cation from B site interacts with octahedral cationic vacancy V'''_B, and oxygen anions interact with oxygen vacancy $V_O^{\bullet\bullet}$. Antistructural modeling can be used for describing solid-solid interactions [61–63], for explanations of the defects in the ferrites system irradiated by γ-rays [64], for catalysts [65, 66], etc.
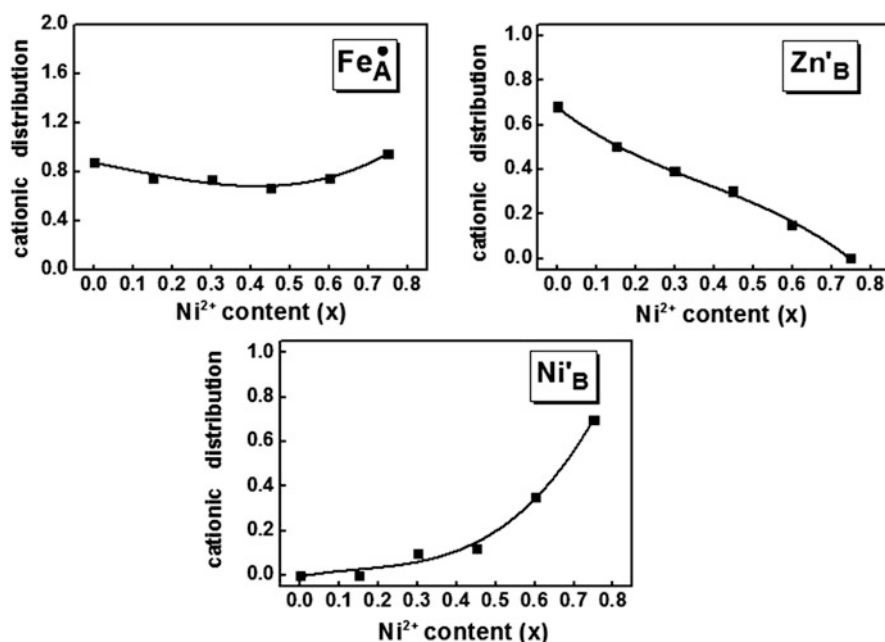
Detail explanation of the interaction between metal cations, oxygen anions, and spinel vacancies, respectively, can be written as $Me_A^{2+}+V''_A \to Me_A^{\times}$; $Me_A^{3+}+V''_A \to Me_A^{\bullet}$; $Me_B^{2+}+V'''_B \to Me_B'$; $Me_B^{3+}+V'''_B \to Me_B^{\times}$; $O^{2-}+V_O^{\bullet\bullet} \to O_O^{\times}$, where × is an effective zero charge. The positive effective charges for electron neutrality reason must be balanced by the equivalent concentration of negative effective charges. In our case, the antistructural modeling, for example, for Ni-doped Mg-Zn-Cu ferrite with $x = 0.45$ can be written as follows:

$$\left(Ni_{0.33}^{2+}Fe_{0.67}^{3+}\right)_A\left[Zn_{0.30}^{2+}Ni_{0.12}^{2+}Mg_{0.15}^{2+}Cu_{0.10}^{2+}Fe_{1.33}^{3+}\right]_B\left(O_4^{2-}\right)_O + \underbrace{V''_A\left[V'''_2\right]_B\left(V_4^{\bullet\bullet}\right)_O}_{\text{spinel antistructure}} \to$$

$$\to \underbrace{\left(Ni_{0.33}^{\times}Fe_{0.67}^{\bullet}\right)_A\left[Zn'_{0.30}Ni'_{0.12}Mg'_{0.15}Cu'_{0.10}Fe_{1.33}^{\times}\right]_B\left(O_4^{\times}\right)_O}_{\text{Ni−doped Zn−Mg−Cu ferrite}}$$

active centres

The antistructural modeling for Ni-doped zinc-magnesium-copper ferrites shown in Table 23.6 gives us new information about the active centers on the ferrite surface. As can be seen from Fig. 23.6, the concentration of positively charged ferric ions in tetrahedral A sites $Fe_A^{\bullet}$ versus nickel ions content first decreases and then increases; the concentration of Zn'_B decreases, while the Ni'_B increases with the Ni content. Antistructural modeling provides us new information about surface-active centers (Table 23.6): Fe_A^{3+}, Zn_B^{2+}, Mg_B^{2+}, Ni_B^{2+}, and Cu_B^{2+} will be active centers in any chemical processes, while Zn_A^{2+}, Cu_A^{2+}, Ni_A^{2+}, and Fe_B^{3+} cations will not be active centers due to their effective zero charge in the crystal lattice.

Table 23.6 Donor and acceptor active centers on the surface of the $Zn_{0.75-x}Ni_xMg_{0.15}Cu_{0.1}Fe_2O_4$ system

Ni (x)	Chemical formulae	Crystalloquasichemical composition
0.00	$Zn^{2+}_{0.75}Mg^{2+}_{0.15}Cu^{2+}_{0.10}Fe^{3+}_{2.0}O^{2-}_4$	$(Zn^{\times}_{0.07}Cu^{\times}_{0.05}Fe^{\bullet}_{0.88})_A[Zn'_{0.68}Mg'_{0.15}Cu'_{0.05}Fe^{\times}_{1.12}]_B(O^{\times}_4)_O$
0.15	$Zn^{2+}_{0.60}Ni^{2+}_{0.15}Mg^{2+}_{0.15}Cu^{2+}_{0.10}Fe^{3+}_{2.0}O^{2-}_4$	$(Zn^{\times}_{0.10}Ni^{\times}_{0.15}Fe^{\bullet}_{0.75})_A[Zn'_{0.50}Mg'_{0.15}Cu'_{0.10}Fe^{\times}_{1.25}]_B(O^{\times}_4)_O$
0.30	$Zn^{2+}_{0.45}Ni^{2+}_{0.30}Mg^{2+}_{0.15}Cu^{2+}_{0.10}Fe^{3+}_{2.0}O^{2-}_4$	$(Zn^{\times}_{0.06}Ni^{\times}_{0.20}Fe^{\bullet}_{0.74})_A[Zn'_{0.39}Ni'_{0.1}Mg'_{0.15}Cu'_{0.10}Fe^{\times}_{1.26}]_B(O^{\times}_4)_O$
0.45	$Zn^{2+}_{0.30}Ni^{2+}_{0.45}Mg^{2+}_{0.15}Cu^{2+}_{0.10}Fe^{3+}_{2.0}O^{2-}_4$	$(Ni^{\times}_{0.33}Fe^{\bullet}_{0.67})_A[Zn'_{0.30}Ni'_{0.12}Mg'_{0.15}Cu'_{0.10}Fe^{\times}_{1.33}]_B(O^{\times}_4)_O$
0.60	$Zn^{2+}_{0.15}Ni^{2+}_{0.60}Mg^{2+}_{0.15}Cu^{2+}_{0.10}Fe^{3+}_{2.0}O^{2-}_4$	$(Ni^{\times}_{0.25}Fe^{\bullet}_{0.75})_A[Zn'_{0.15}Ni'_{0.35}Mg'_{0.15}Cu'_{0.10}Fe^{\times}_{1.25}]_B(O^{\times}_4)_O$
0.75	$Ni^{2+}_{0.75}Mg^{2+}_{0.15}Cu^{2+}_{0.10}Fe^{3+}_{2.0}O^{2-}_4$	$(Ni^{\times}_{0.05}Fe^{\bullet}_{0.95})_A[Ni'_{0.70}Mg'_{0.15}Cu'_{0.10}Fe^{\times}_{1.05}]_B(O^{\times}_4)_O$

Fig. 23.6 Concentration of active surface centers in tetrahedral A sites (Fe) and octahedral B sites (Zn, Ni) as a function of the Ni^{2+} content (x) for $Zn_{0.75-x}Ni_xMg_{0.15}Cu_{0.1}Fe_2O_4$ samples

23.4 Conclusions

Ni addition induced changes in structural, magnetic properties, morphology, and cationic distribution of ann. Zn-Ni-Mg-Cu ferrite is studied in this paper. X-ray diffraction pattern of annealed (500 °C/3 h) $Zn_{0.75-x}Ni_xMg_{0.15}Cu_{0.1}Fe_2O_4$ ferrite with $x = 0.0, 0.15, 0.30, 0.45, 0.60,$ and 0.75 synthesized by sol-gel auto-combustion

technique gives a clear indication of formation of cubic spinel phase with Scherrer's grain diameter (D) ranging: 41.40–56.73 nm. Lattice parameter ($a_{\text{exp.}}$) and hopping length for A and B site (L_A, L_B) decrease with Ni addition, accredited to the replacement of Zn^{2+} by Ni^{2+} ions. Ni addition induced variation in tetrahedral bond length (R_A) and is in agreement with changes in the ionic radii of A site (r_A). Decrease in octahedral bond length (R_B) and shared and unshared octahedral edge (d_{BE}, d_{BEu}) with Ni addition is accredited to the replacement of larger ion (Zn^{2+}) by smaller ion (Ni^{2+}). SEM images clearly show porous structure of the sample: $x = 0.00$. With Ni addition, coercivity (H_c) and squareness ratio (M_r/M_s) increase. The magnetic parameters, Néel and experimental magnetic moment ($n^e{}_N$, $n^e{}_B$) μ_B, saturation magnetization (M_s), and magneto-crystalline anisotropy constant (K_1), increase for lower Ni content ($0.00 \leq x \leq 0.45$) and reduce for higher Ni content ($0.45 < x \leq 0.75$). Non-zero Yafet-Kittel angle ($\alpha_{Y\text{-}K}$) suggests presence of Yafet-Kittel type of magnetic ordering in $Zn_{0.75-x}Ni_xMg_{0.15}Cu_{0.1}Fe_2O_4$ (ann. 500 °C/3 h) system. A new antistructural modeling for describing active surface centers for Ni-doped zinc-magnesium-copper ferrites system is discussed for the first time.

References

1. Zhang H, Ma Z, Zhou J et al (2000) Preparation and investigation of $(Ni_{0.15}Cu_{0.25}Zn_{0.60})Fe_{1.96}O_4$ ferrite with very high initial permeability from self-propagated powders. J Magn Magn Mater 213:304–308
2. Reddy MP, Madhuri W, Ramana MV et al (2010) Effect of sintering temperature on structural and magnetic properties of NiCuZn and MgCuZn ferrites. J Magn Magn Mater 322:2819–2823
3. Reddy MP, Madhuri W, Balakrishnaiah G et al (2011) Microwave sintering of iron deficient Ni–Cu–Zn ferrites for multilayer chip inductors. Curr Appl Phys 11:191–198
4. Costa ACFM, Lula RT, Kiminami RHGA et al (2006) Preparation of nanostructured NiFe₂O₄ catalysts by combustion reaction. J Mater Sci 41:4871–4875
5. Dey C, Baishya K, Ghosh A et al (2017) Improvement of drug delivery by hyperthermia treatment using magnetic cubic cobalt ferrite nanoparticles. J Magn Magn Mater 427:168–174. https://doi.org/10.1016/j.jmmm.2016.11.024
6. Tartaj P, Morales MP, Verdaguer SV et al (2003) The preparation of magnetic nanoparticles for applications in biomedicine. J Phys D Appl Phys 36:R182–R197
7. Azad AM, Hedayati A, Rydn M et al (2013) Examining the Cu–Mn–O spinel system as an oxygen carrier in chemical looping combustion. Energy Technol 1:59–69
8. Reddy DHK, Yun Y-S (2016) Spinel ferrite magnetic adsorbents: alternative future materials for water purification? Coord Chem Rev 315:90–111
9. Ehrhardt H, Campbell SJ, Hofmann M (2002) Structural evolution of ball-milled ZnFe₂O₄. J Alloys Compd 339:255–260
10. Sepelak V, Baabe D, Mienert D et al (2003) Evolution of structure and magnetic properties with annealing temperature in nanoscale high-energy-milled nickel ferrite. J Magn Magn Mater 257:377–386

11. Ammar S, Jouini N, Fiévet F et al (2004) Influence of the synthesis parameters on the cationic distribution of $ZnFe_2O_4$ nanoparticles obtained by forced hydrolysis in polyol medium. J Non-Cryst Solids 345:658–662

12. Willard MA, Nakamura Y, Laughlin DE et al (1999) Magnetic properties of ordered and disordered spinel-phase ferrimagnets. J Am Ceram Soc 82:3342–3346

13. Smit J, Wijn HPJ (1959) Ferrites. Philips' Technical Library, Eindhoven-Netherlands, pp 148–149, 157

14. Chikazumi S (1997) Physics of ferromagnetism. Oxford University Press, Oxford, pp 502–504

15. Roy PK, Bera J (2006) Effect of Mg substitution on electromagnetic properties of $(Ni_{0.25}Cu_{0.20}Zn_{0.55})$ Fe_2O_4 ferrite prepared by auto combustion method. J Magn Magn Mater 298:38–42

16. Sujatha C, Reddy KV, Babu KS et al (2013) Effect of Mg substitution on electromagnetic properties of NiCuZn ferrite. J Magn Magn Mater 340:38–45

17. Akther Hossain AKM, Biswas TS, Yanagida T et al (2010) Investigation of structural and magnetic properties of polycrystalline $Ni_{0.50}Zn_{0.50-x}Mg_xFe_2O_4$ spinel ferrites. Mater Chem Phys 120:461–467

18. Varalaxmi N, Reddy NR, Ramana MV et al (2008) Stress sensitivity of inductance in NiMgCuZn ferrites and development of a stress insensitive ferrite composition for micro inductors. J Mater Sci Mater Electron 19:399–405

19. Dar MA, Verma V, Gairola SP et al (2012) Low dielectric loss of Mg doped Ni–Cu–Zn nano-ferrites for power applications. Appl Surf Sci 258:5342–5347

20. Sujatha C, Reddy KV, Babu KS et al (2012) Structural and magnetic properties of Mg substituted NiCuZn nano ferrites. Physica B 407:1232–1237

21. Sujatha C, Reddy KV, Babu KS et al (2013) Effect of co substitution of Mg and Zn on electromagnetic properties of NiCuZn ferrites. J Phys Chem Solids 74:917–923

22. Satalkar M, Kane SN, Ghosh A et al (2014) Synthesis and soft magnetic properties of $Zn_{0.8-x}Ni_xMg_{0.1}Cu_{0.1}Fe_2O_4$ (x = 0.0–0.8) ferrites prepared by sol-gel auto-combustion method. J Alloys Compd 615:S313–S316

23. Kane SN, Satalkar M (2017) Correlation between magnetic properties and cationic distribution of $Zn_{0.85-x}Ni_xMg_{0.05}Cu_{0.1}Fe_2O_4$ nano spinel ferrite: effect of Ni doping. J Mater Sci 52:3467–3477

24. Satalkar M, Kane SN, Kumaresavanji M et al (2017) On the role of cationic distribution in determining magnetic properties of $Zn_{0.7-x}Ni_xMg_{0.2}Cu_{0.1}Fe_2O_4$ nano ferrite. Mater Res Bull 91:14–21. https://doi.org/10.1016/j.materresbull.2017.03.021

25. Rana MU, Misbah-ul-Islam, Abbas T (2003) Magnetic interactions in Cu-substituted manganese ferrites. Solid State Commun 126:129–133

26. Topkaya R, Baykal A, Demir A (2013) Yafet–Kittel-type magnetic order in Zn-substituted cobalt ferrite nanoparticles with uniaxial anisotropy. J Nanopart Res 15:1359–1376

27. Bamzai KK, Kour G, Kaur B et al (2014) Preparation, and structural and magnetic properties of Ca substituted magnesium ferrite with composition $MgCa_xFe_{2-x}O4$ (x = 0.00, 0.01, 0.03, 0.05, 0.07). J Mater 2014:1–8

28. Mazen SA, Abu-Elsaad NI (2006) Structural and some magnetic properties of manganese-substituted lithium ferrites. J Magn Magn Mater 298:38–42

29. Gadkari AB, Shinde TJ, Vasambekar PN (2010) Magnetic properties of rare earth ion (Sm^{3+}) added nanocrystalline Mg–Cd ferrites, prepared by oxalate co-precipitation method. J Magn Magn Mater 322:3823–3827

30. Jadhav SA (2001) Magnetic properties of Zn-substituted Li–Cu ferrites. J Magn Magn Mater 224:167–172

31. Kapse VD, Ghosh SA, Raghuwanshi FC et al (2009) Nanocrystalline spinel $Ni_{0.6}Zn_{0.4}Fe_2O_4$: A novel material for H_2S sensing. Mater Chem Phys 113:638–644

32. Lutterotti L, Scardi P (1990) Simultaneous structure and size-strain refinement by the Rietveld method. J Appl Crystallogr 23:246–252

33. Qi X, Zhou J, Yue Z et al (2003) Permeability and microstructure of manganese modified lithium ferrite prepared by sol–gel auto-combustion method. Mater Sci Eng B 99:278–281

34. Mohammed KA, Al-Rawas AD, Gismelseed AM et al (2012) Infrared and structural studies of $Mg_{1-x}Zn_xFe_2O_4$ ferrites. Physica B 407:795–804

35. Alone ST, Shirsath SE, Kadam RH et al (2011) Chemical synthesis, structural and magnetic properties of nano-structured Co–Zn–Fe–Cr ferrite. J Alloys Compd 509:5055–5060

36. Vegard L (1921) The constitution of mixed crystals and the space occupied by atoms. Z Phys 5:17–26

37. Sharma R, Thakur P, Sharma P et al (2017) Ferrimagnetic Ni^{2+} doped Mg-Zn spinel ferrite nanoparticles for high density information storage. J Alloys Compd 704:7–17

38. Weil L, Bertaut EF, Bochirol L (1950) Propriétés magnétiques et structure de la phase quadratique du ferrite de cuivre. J Phys Radium 11:208–212

39. Eloska E, Wolski W (1992) The evidence of $Cd_x{}^{2+}Fe_{1-x}{}^{3+}[Ni^{2+}{}_{1-x}Fe^{3+}{}_{1+x}]O_4$ cation distribution based on X-ray and mossbauer data. Phys Status Solidi (A) 132:K51–K56

40. Cervinka L, Simsa Z (1970) Distribution of copper ions in some copper-manganese ferrites. J Phys B (Czechoslovakia) 20:470–474

41. Tanna AR, Joshi HH (2013) Computer aided X-ray diffraction intensity analysis for spinels: hands-on computing experience. World Acad Sci Eng Technol 75:334–341

42. Pandit AA, More SS, Dorik RG et al (2003) Structural and magnetic properties of $Co_{1+y}Sn_yFe_{2-2y-x}Cr_xO_4$ ferrite system. Bull Mater Sci 26:517–521

43. Al-Hilli MF, Li S, Kassim KS (2012) Structural analysis, magnetic and electrical properties of samarium substituted lithium–nickel mixed ferrites. J Magn Magn Mater 324:873–879

44. Alimuddin MH, Shirsath SE, Meena SS et al (2013) Investigation of structural, dielectric, magnetic and antibacterial activity of Cu–Cd–Ni–FeO_4 nanoparticles. J Magn Magn Mater 341:148–157

45. Hashim M, Meena SS, Kotnala RK et al (2014) Exploring the structural, Mössbauer and dielectric properties of Co^{2+} incorporated $Mg_{0.5}Zn_{0.5-x}Co_xFe_2O_4$ nanocrystalline ferrite. J Magn Magn Mater 360:21–33

46. Mustafa G, Islam MU, Zhang W et al (2015) Influence of the divalent and trivalent ions substitution on the structural and magnetic properties of $Mg_{0.5-x}Cd_xCo_{0.5}Cr_{0.04}Tb_yFe_{1.96-y}O_4$ ferrites prepared by sol–gel method. J Magn Magn Mater 387:147–154

47. Mohamed MB, Wahba AM, Heiba ZK (2015) Effect of Zn substitution on structural, magnetic, and electric properties of $Ni_{1-x}Zn_xFe_{1.78}Al_{0.2}Gd_{0.02}O_4$ nanoparticles. J Supercond Nov Magn 28:3675–3683

48. Sathishkumar G, Venkataraju C, Sivakumar K (2013) Magnetic and dielectric properties of cadmium substituted nickel cobalt nanoferrites. J Mater Sci Mater Electron 24:1057–1062

49. Najmoddin N, Beitollahi A, Kavas H et al (2014) XRD cation distribution and magnetic properties of mesoporous Zn-substituted $CuFe_2O_4$. Ceram Int 40:3619–3625

50. Jadhav J, Biswas S, Yadav AK et al (2017) Structural and magnetic properties of nanocrystalline Ni-Zn ferrites: in the context of cationic distribution. J Alloys Compd 696:28–41

51. Kurmude DV, Barkule RS, Raut AV et al (2014) X-ray diffraction and cation distribution studies in zinc-substituted nickel ferrite nanoparticles. J Supercond Nov Magn 27:547–553

52. Tholkappiyan R, Vishista K (2015) Combustion synthesis of Mg–Er ferrite nanoparticles: cation distribution and structural, optical, and magnetic properties. Mater Sci Semicond Process 40:631–642

53. Sutka A, Mezinskis G (2012) Sol–gel auto-combustion synthesis of spinel-type ferrite nanomaterials. Front Mater Sci 6:128–141

54. Sun Y, Ji G, Zheng M et al (2010) Synthesis and magnetic properties of crystalline mesoporous $CoFe_2O_4$ with large specific surface area. J Mater Chem 20:945–952

55. Rikukawa H (1982) Relationship between microstructures and magnetic properties of ferrites containing closed pores. IEEE Trans Magn 18:1535–1537

56. Gao Z, Cui F, Zeng S et al (2010) A high surface area superparamagnetic mesoporous spinel ferrite synthesized by a template-free approach and its adsorptive property. Microporous Mesoporous Mater 132:188–195

57. Verma A, Chatterjee R (2006) Effect of zinc concentration on the structural, electrical and magnetic properties of mixed Mn–Zn and Ni–Zn ferrites synthesized by the citrate precursor technique. J Magn Magn Mater 306:313–320
58. Yafet Y, Kittel C (1952) Antiferromagnetic arrangements in ferrites. Phys Rev 87:290–294
59. Raghuvanshi S, Mazaleyrat F, Kane SN (2018) $Mg_{1-x}Zn_xFe_2O_4$ nanoparticles: interplay between cation distribution and magnetic properties. AIP Adv 8:047804–047810
60. Faraz A, Maqsood A (2012) Synthesis, structural, electrical, magnetic Curie temperature and Y–K angle studies of Mn–Cu–Ni mixed spinel nanoferrites. J Supercond Nov Magn 25:509–517
61. Tatarchuk TR, Paliychuk ND, Bououdina M et al (2018) Effect of cobalt substitution on structural, elastic, magnetic and optical properties of zinc ferrite nanoparticles. J Alloys Compd 731:1256–1266. https://doi.org/10.1016/j.jallcom.2017.10.103
62. Tatarchuk T, Bououdina M, Macyk W et al (2017) Structural, optical, and magnetic properties of Zn-doped $CoFe_2O_4$ nanoparticles. Nanoscale Res Lett 12(1):141–151. https://doi.org/10.1186/s11671-017-1899-x
63. Tatarchuk T, Bououdina M, Paliychuk N et al (2017) Structural characterization and antistructure modeling of cobalt-substituted zinc ferrites. J Alloys Compd 694:777–791. https://doi.org/10.1016/j.jallcom.2016.10.067
64. Ahmed MA, Hassan HE, Eltabey MM et al (2018) Mössbauer spectroscopy of $Mg_xCu_{0.5-x}Zn_{0.5}Fe_2O_4$ (x=0.0, 0.2 and 0.5) ferrites system irradiated by γ-rays. Phys B Condens Matter 530:195–200. https://doi.org/10.1016/j.physb.2017.10.125
65. Kurta SA, Mykytyn IM, Tatarchuk TR (2014) Structure and the catalysis mechanism of oxidative chlorination in nanostructural layers of a surface of alumina. Nanoscale Res Lett 9(1):357–365. https://doi.org/10.1186/1556-276X-9-357
66. Tatarchuk T, Bououdina M, Vijaya JJ et al (2017) Spinel ferrite nanoparticles: synthesis, crystal structure, properties, and perspective applications. In: Fesenko O, Yatsenko L (eds) Nanophysics, nanomaterials, interface studies, and applications. NANO 2016. Springer Proceedings in Physics, vol 195. Springer, Cham, pp 305–325. https://doi.org/10.1007/978-3-319-56422-7_22